TOI-1842b: A Transiting Warm Saturn Undergoing Reinflation Around An Evolving Subgiant

R. A. Wittenmyer

J. T. Clark

T. Trifonov

See next page for additional authors

Authors

R. A. Wittenmyer, J. T. Clark, T. Trifonov, B. C. Addison, D. J. Wright, K. G. Stassun, J. Horner, N. Lowson, J. Kielkopf, S. R. Kane, P. Plavchan, A. Shporer, H. Zhang, B. P. Bowler, M. W. Mengel, J. Okumura, M. Rabus, M. C. Johnson, D. Harbeck, R. Tronsgaard, L. A. Buchhave, K. A. Collins, K. I. Collins, T. Gan, Eric L.N. Jensen, S. B. Howell, E. Furlan, C. L. Gnilka, K. V. Lester, R. A. Matson, N. J. Scott, G. R. Ricker, R. Vanderspek, D. W. Latham, S. Seager, J. N. Winn, J. M. Jenkins, A. Rudat, E. V. Quintana, D. R. Rodriguez, D. A. Caldwell, S. N. Quinn, Z. Essack, and L. G. Bouma

TOI-1842b: A Transiting Warm Saturn Undergoing Reinflation around an Evolving Subgiant

Robert A. Wittenmyer[1] , Jake T. Clark[1] , Trifon Trifonov[2] , Brett C. Addison[1] , Duncan J. Wright[1] , Keivan G. Stassun[3] ,
Jonathan Horner[1] , Nataliea Lowson[1] , John Kielkopf[4] , Stephen R. Kane[5] , Peter Plavchan[6] , Avi Shporer[7] ,
Hui Zhang[8] , Brendan P. Bowler[9] , Matthew W. Mengel[10] , Jack Okumura[10] , Markus Rabus[11,12,13] ,
Marshall C. Johnson[12] , Daniel Harbeck[12] , René Tronsgaard[14] , Lars A. Buchhave[14] , Karen A. Collins[15] ,
Kevin I. Collins[6] , Tianjun Gan[16] , Eric L. N. Jensen[17] , Steve B. Howell[18] , E. Furlan[19] , Crystal L. Gnilka[18] ,
Kathryn V. Lester[18] , Rachel A. Matson[20] , Nicholas J. Scott[18] , George R. Ricker[7] , Roland Vanderspek[7] ,
David W. Latham[21] , S. Seager[7,22,23], Joshua N. Winn[24] , Jon M. Jenkins[18] , Alexander Rudat[7], Elisa V. Quintana[25],
David R. Rodriguez[26] , Douglas A. Caldwell[18,27] , Samuel N. Quinn[15] , Zahra Essack[22,28] , and Luke G. Bouma[29]

[1] University of Southern Queensland, Centre for Astrophysics, USQ Toowoomba, West Street, QLD 4350 Australia; rob.w@usq.edu.au
[2] Max-Planck-Institut fur Astronomie, Konigstuhl 17, D-69117 Heidelberg, Germany
[3] Vanderbilt University, Department of Physics & Astronomy, Nashville, TN 37235, USA
[4] Department of Physics and Astronomy, University of Louisville, Louisville, KY 40292, USA
[5] Department of Earth and Planetary Sciences, University of California, Riverside, CA 92521, USA
[6] Department of Physics & Astronomy, George Mason University, 4400 University Drive MS 3F3, Fairfax, VA 22030, USA
[7] Department of Physics and Kavli Institute for Astrophysics and Space Research, Massachusetts Institute of Technology, Cambridge, MA 02139, USA
[8] School of Astronomy and Space Science, Key Laboratory of Modern Astronomy and Astrophysics in Ministry of Education, Nanjing University, Nanjing 210046,
Jiangsu, People's Republic of China
[9] Department of Astronomy, The University of Texas at Austin, Austin, TX 78712, USA
[10] University of Southern Queensland, Centre for Astrophysics, West Street, Toowoomba, QLD 4350 Australia
[11] Departamento de Matemática y Física Aplicadas, Universidad Católica de la Santísima Concepción, Alonso de Rivera 2850, Concepción, Chile
[12] Las Cumbres Observatory, 6740 Cortona Drive, Suite 102, Goleta, CA 93117, USA
[13] Department of Physics, University of California, Santa Barbara, CA 93106-9530, USA
[14] DTU Space, National Space Institute, Technical University of Denmark, Elektrovej 328, DK-2800 Kgs. Lyngby, Denmark
[15] Center for Astrophysics | Harvard & Smithsonian, 60 Garden Street, Cambridge, MA 02138, USA
[16] Department of Astronomy and Tsinghua Centre for Astrophysics, Tsinghua University, Beijing 100084, People's Republic of China
[17] Department of Physics & Astronomy, Swarthmore College, Swarthmore PA 19081, USA
[18] NASA Ames Research Center, Moffett Field, CA 94035, USA
[19] NASA Exoplanet Science Institute, Caltech/IPAC, Mail Code 100-22, 1200 E. California Boulevard, Pasadena, CA 91125, USA
[20] U.S. Naval Observatory, 3450 Massachusetts Avenue NW, Washington, DC 20392, USA
[21] Center for Astrophysics | Harvard & Smithsonian, 60 Garden Street, Cambridge, MA 02138, USA
[22] Department of Earth, Atmospheric and Planetary Sciences, Massachusetts Institute of Technology, Cambridge, MA 02139, USA
[23] Department of Aeronautics and Astronautics, MIT, 77 Massachusetts Avenue, Cambridge, MA 02139, USA
[24] Department of Astrophysical Sciences, Princeton University, Princeton, NJ 08540, USA
[25] NASA Goddard Space Flight Center, 8800 Greenbelt Road, Greenbelt, MD 20771, USA
[26] Space Telescope Science Institute, 3700 San Martin Drive, Baltimore, MD, 21218, USA
[27] SETI Institute, Mountain View, CA 94043, USA
[28] Kavli Institute for Astrophysics and Space Research, Massachusetts Institute of Technology, Cambridge, MA 02139, USA
[29] Department of Astrophysical Sciences, Princeton University, 4 Ivy Lane, Princeton, NJ 08544, USA

Abstract

The imminent launch of space telescopes designed to probe the atmospheres of exoplanets has prompted new efforts to prioritize the thousands of transiting planet candidates for follow-up characterization. We report the detection and confirmation of TOI-1842b, a warm Saturn identified by TESS and confirmed with ground-based observations from MINERVA-Australis, NRES, and the Las Cumbres Observatory Global Telescope. This planet has a radius of $1.04^{+0.06}_{-0.05}\,R_J$, a mass of $0.214^{+0.040}_{-0.038}\,M_J$, an orbital period of $9.5739^{+0.0002}_{-0.0001}$ days, and an extremely low density ($\rho = 0.252 \pm 0.091$ g cm^{-3}). TOI-1842b has among the best known combinations of large atmospheric scale height (893 km) and host-star brightness ($J = 8.747$ mag), making it an attractive target for atmospheric characterization. As the host star is beginning to evolve off the main sequence, TOI-1842b presents an excellent opportunity to test models of gas giant reinflation. The primary transit duration of only 4.3 hr also makes TOI-1842b an easily-schedulable target for further ground-based atmospheric characterization.

Unified Astronomy Thesaurus concepts: Exoplanet detection methods (489); Transit photometry (1709); Radial velocity (1332); Extrasolar gaseous giant planets (509)

1. Introduction

The tireless efforts of exoplanetary astronomers have, for more than three decades, relentlessly banished the darkness shrouding the mysteries of planetary system formation and evolution in the Solar neighborhood. The stars that our ancestors once thought of as distant campfires are now known to host retinues of worlds in a

riotous array of sizes, compositions, and orbital properties. Of late, we have fueled this revolution with deceptively small space-borne robotic sentries; the Kepler (Borucki et al. 2010) and now Transiting Exoplanet Survey Satellite (TESS; Ricker et al. 2015) spacecraft have delivered 2981 new confirmed exoplanets from over 6000 candidates.[30]

The Level 1 mission requirement of TESS is to obtain mass and radius measurements for 50 planets smaller than 4 $R_\oplus$(Ricker et al. 2015), and at the end of its two-year prime mission in 2020 July, nearly 40 such Level 1 planets have been confirmed (e.g., Huang et al. 2018; Luque et al. 2019; Quinn et al. 2019; Vanderburg et al. 2019; Trifonov et al. 2021). As is common in astronomy, where the most attention is lavished on discoveries at the margins of detectability, transits of larger planets are often overshadowed by their smaller kin. However, such warm giants from the TESS mission are also scientifically valuable (e.g., Nielsen et al. 2019; Dalba et al. 2020; Jordán et al. 2020; Schlecker et al. 2020). These giant planets, with orbital periods between about 5 and 10 days, reside far enough from their host star that tidal circularization has not yet erased any orbital eccentricity or inclination imposed by postformation migration mechanisms (Dawson & Johnson 2018). Such planets are thus important laboratories for understanding the means by which close-in giant planets are delivered to their present locations.

In a similar vein, planets orbiting stars of different types than the Sun remain underrepresented. This arose first from the technical requirements of the radial-velocity method, which favored Solar-type stars (late F through K dwarfs) due to the Doppler information contained within their abundant and narrow spectral lines (e.g., Mayor & Queloz 1995; Cochran et al. 1997; Butler et al. 1999; Pepe et al. 2004; Vogt et al. 2010). As the transit technique flowered in the age of Kepler, the bias toward Solar-type stars was reinforced to give the mission the best chance of achieving its goal of detecting Earth-size planets. Again, the hotter and more evolved stars were spurned for their younger and cooler counterparts. Evolved stars in particular are heavily disfavored in transit searches since their larger stellar radii diminish the transit signals of planets. The advent of purpose-built infrared high-precision spectrographs (Mahadevan et al. 2012; Quirrenbach et al. 2014; Kotani et al. 2018; Gilbert et al. 2018) has fueled an outsized interest in the coolest stars, stoked heavily by the profligacy with which the universe produces systems of multiple small planets around these M dwarfs (e.g., Anglada-Escudé et al. 2012; Wright et al. 2016; Dreizler et al. 2020; Cloutier et al. 2019), and because habitable-zone planets are more accessible.

However, the hotter, higher-mass stars (A type through mid-F dwarfs) have yet to receive much attention from the exoplanet community. While on the main sequence, these stars offer a limited number of useful spectral lines for radial-velocity measurement. Some progress toward understanding the exoplanet population hosted by these stars has been achieved by studying their evolved counterparts, since, as subgiants and low-luminosity giants, the stars cool down and slow their rotation, resulting in a forest of narrow spectral lines that permit precise velocity measurements (e.g., Johnson et al. 2007; Bowler et al. 2010; Jones et al. 2011; Sato et al. 2013; Wittenmyer et al. 2020). A conundrum has been the apparent lack of giant planets in orbits shorter than ∼100 days

(Johnson et al. 2010; Reffert et al. 2015; Van Eylen et al. 2016; Jones et al. 2021). Contrary to popular belief, the hot- and warm-Jupiter populations have not been engulfed by gastronomically rapacious host stars—the low-luminosity giants targeted by the major surveys have typical radii of less than 10 $R_\odot$, so close-in giant planets would remain intact until the last ∼1% of their lifetimes (Villaver & Livio 2009; Kunitomo et al. 2011). Transit surveys have been successful in confirming the presence of close-in giant planets around main-sequence A and F stars (e.g., Snellen et al. 2009; Talens et al. 2017; Rodriguez et al. 2019), and preliminary estimates of the occurrence rates suggest that there is no significant dependence on host-star mass (Zhou et al. 2019).

In this paper, we report the discovery and confirmation of TOI-1842b, a rare short-period giant planet orbiting an evolved star. Section 2 details the various photometric and spectroscopic observations, and in Section 3, we describe the properties of the host star. Section 4 gives the results of the joint fitting, and we conclude in Section 5.

2. Observations and Data Reduction

In this section, we describe the TESS photometry, follow-up ground-based photometry, and spectroscopic observations used to establish the planetary nature of TOI-1842b.

2.1. Photometric Observations

2.1.1. TESS Light Curve

TOI-1842 (TIC 404505029, Stassun et al. 2019) was observed by TESS on Camera 1 in Sector 23 in 2 minutes cadence mode nearly continuously between 2020 March 19 and 2020 April 15. The TESS Science Processing Operations Center (SPOC) pipeline (see Jenkins et al. 2016 for a description of the SPOC pipeline) was used to process the photometric data, resulting in two versions of the light curves: Simple Aperture Photometry (SAP; Twicken et al. 2010; Morris et al. 2020) and Presearch Data Conditioning (PDC; Stumpe et al. 2012, 2014; Smith et al. 2012). Both versions of the light curves were downloaded from the NASA's Mikulski Archive for Space Telescopes for analysis. The SPOC conducted a transit search of the PDC light curve with an adaptive, noise-compensating matched filter (Jenkins 2002; Jenkins et al. 2010), triggering on two transits of TOI-1842b. No additional transiting planet signatures were identified in a search of the residual light curve.

The transiting planet candidate was released as a candidate TESS Object of Interest (TOI) and designated TOI-1842.01 by the TESS Science Office based on model-fit results and a passing grade on all diagnostic tests in the SPOC data validation (DV) report (Twicken et al. 2018; Li et al. 2019) for Sector 23. These diagnostic tests included a difference image centroiding analysis that located the source of the transit signature to within $1{\overset{''}{.}}6 \pm 2{\overset{''}{.}}5$ of TOI-1842. In total, two transits were observed by TESS with a duration of ∼4.4 hr, a depth of ∼3150 parts per million (ppm), and a period of ∼9.57 days, with the first detected transit occurring on BJD$_{\text{TDB}}$ 2458933. Joint analysis (see Section 4) of the radial-velocity data, TESS light curve, and ground-based follow-up light curve from the Las Cumbres Observatory Global Telescope (LCOGT) confirm that the planet has a period of ∼9.57 days (half the original period published in the SPOC DV report of

---

[30] Planet data from the NASA Exoplanet Archive at https://exoplanetarchive.ipac.caltech.edu/, accessed 2021 August 25.

~19.15 days), resulting in one transit being missed by TESS during the data downlink gap as shown in Figure 5.

We removed all quality-flagged data from the SAP and PDC light curves before detrending and fitting them. The light curves were then split into a total of four segments, with each segment split at the spacecraft momentum dumps[31] that occurred 8.0 days after the beginning of each orbit, to minimize the offset effects on the light curves during the fitting analysis. The transits were then masked and a 5σ median filter was applied to the out-of-transit data to remove remaining outliers in each light-curve segment. After masking the transits and applying a median filter, we detrended each light-curve segment using an rspline with iterative sigma clipping and a filter window set to 4.0 times the planet period using the Python package Wōtan (Hippke et al. 2019). Lastly, the light-curve segments were normalized with the mean of the out-of-transit flux before performing the fitting analysis as described in Section 4. In the joint fit, we choose the detrended PDC light curve over the detrended SAP light curve as it has already been corrected for instrumental and systematic effects as well as for light dilution by the SPOC pipeline.

2.1.2. Las Cumbres Observatory

We obtained three transits of TOI-1842.01 in Pan-STARSS z-short band with an exposure time of 30 s on UTC 2020 May 30, 2021 February 13, and 2021 April 2 from LCOGT (Brown et al. 2013) 1.0 m network nodes. The first photometric observation was taken at the South Africa Astronomical Observatory while the latter two were done at the Cerro Tololo Interamerican Observatory. We used the TESS Transit Finder, which is a customized version of the Tapir software package (Jensen 2013), to schedule our transit observations. The first transit was scheduled using a period of 9.5740475 days (half the original period), and on an epoch that corresponds to a possibly missed transit in the TESS data gap (see Section 2.1.1). The 4096×4096 LCOGT SINISTRO cameras have an image scale of $0\rlap{.}''389$ per pixel, resulting in a $26' \times 26'$ field of view. The images were calibrated by the standard LCOGT BANZAI pipeline (McCully et al. 2018), and photometric data were extracted using AstroImageJ (Collins et al. 2017). The images were defocused and have typical stellar point-spread functions with a full width half maximum of $\sim 5\rlap{.}''7$, and circular apertures with radius $\sim 6\rlap{.}''6$ were used to extract the differential photometry. A transit with depth ~ 3000 ppm was detected on target, showing that the true period is half the originally published ~ 19.1 day period (see Section 4). The latter two follow-up observations confirmed the return of the signal on target and at the 9.57 days period.

2.2. Spectroscopic Observations

TOI-1842 has been observed by three facilities for stellar parameter determination and precise radial-velocity follow up. Here we give details about the observations from each instrument. All radial velocities used in this analysis are given in Table 1.

2.2.1. MINERVA-Australis

We carried out the spectroscopic observations of TOI-1842 using the MINERVA-Australis facility (Wittenmyer et al. 2018;

Table 1
Radial Velocities for TOI-1842

Time (BJD)	Velocity (m s^{-1})	Uncertainty (m s^{-1})	Fiber/Telescope
MINERVA-Australis			
2458981.99578	3730.8	17.4	4
2458982.03844	3654.9	15.5	4
2458995.05865	3677.3	12.6	4
2458995.05865	3695.3	10.1	5
2458995.10137	3667.2	13.5	4
2458995.10137	3670.7	11.8	5
2458996.01626	3669.3	12.6	4
2458996.01626	3700.1	9.3	5
2458996.05897	3616.9	17.1	4
2458996.05897	3667.9	13.9	5
2458997.97378	3703.6	12.3	5
2458997.97378	3725.2	15.1	4
2458998.01650	3709.2	11.8	4
2458998.01650	3713.9	9.1	5
2458998.87519	3629.3	11.9	1
2458998.87519	3669.8	10.6	4
2458998.87519	3742.2	10.9	5
2458998.91789	3646.5	10.0	1
2458998.91789	3687.4	11.2	4
2458998.91789	3694.1	9.1	5
2458999.87477	3623.5	12.1	1
2458999.87477	3678.9	11.2	4
2458999.87477	3690.6	10.4	5
2458999.91749	3647.2	10.7	1
2458999.91749	3675.0	10.8	4
2458999.91749	3704.5	9.1	5
2459000.87519	3664.1	13.8	5
2459000.87519	3667.9	15.0	4
2459000.91791	3683.9	10.6	5
2459000.91791	3689.3	13.2	4
2459001.87494	3658.3	19.0	4
2459001.87494	3691.3	15.4	5
2459001.91766	3642.7	13.5	5
2459001.91766	3695.1	21.4	4
2459002.87503	3672.1	9.7	5
2459002.87503	3680.8	14.1	4
2459002.95885	3614.2	8.9	1
2459002.95885	3665.9	9.4	5
2459002.95885	3693.0	16.6	4
2459003.00157	3585.6	8.6	1
2459003.00157	3628.5	13.4	4
2459003.00157	3663.3	9.5	5
2459003.96260	3602.3	8.8	1
2459003.96260	3667.6	13.2	4
2459003.96260	3672.4	9.2	5
2459004.00531	3596.1	8.8	1
2459004.00531	3669.9	13.3	4
2459004.00531	3683.0	9.5	5
2459004.04903	3623.1	9.3	1
2459004.04903	3651.2	13.7	4
2459004.04903	3695.8	9.5	5
2459005.88421	3629.4	9.5	1
2459005.88421	3702.1	8.9	5
2459005.92693	3639.4	9.1	1
2459005.92693	3705.7	8.6	5
2459006.87339	3649.4	15.2	1
2459006.87339	3703.0	11.9	5
2459006.87339	3716.6	21.2	4
2459006.91611	3614.4	43.2	4
2459006.91611	3628.9	16.5	1
2459006.91611	3717.5	11.4	5
2459008.87830	3699.9	14.7	1
2459008.87830	3713.8	8.8	5
2459008.92102	3646.0	10.2	1
2459008.92102	3681.5	8.3	5
2459015.87987	3680.3	9.7	5
2459017.98362	3637.8	9.1	1
2459017.98362	3692.8	9.2	5
2459017.98362	3698.2	12.2	4
2459022.89711	3658.2	11.1	1

Table 1
(Continued)

Time (BJD)	Velocity (m s^{-1})	Uncertainty (m s^{-1})	Fiber/Telescope
2459022.89711	3665.3	12.6	4
2459022.89711	3679.3	9.4	5
2459022.93984	3589.5	9.2	1
2459022.93984	3679.9	9.2	5
2459022.93984	3684.7	12.2	4
2459023.93098	3619.7	13.1	4
2459023.93098	3673.0	9.2	5
2459024.95263	3619.9	8.2	1
2459024.95263	3667.9	12.5	4
2459024.95263	3697.6	9.1	5
2459024.99541	3631.9	8.7	1
2459024.99541	3678.1	11.9	4
2459024.99541	3715.8	9.1	5
2459025.90669	3688.4	12.8	4
2459025.90669	3689.3	8.9	5
2459025.94941	3691.3	13.3	4
2459025.94941	3701.4	9.0	5
2459026.91155	3622.5	8.4	1
2459026.91155	3653.9	15.3	4
2459026.91155	3694.2	8.9	5
2459026.95427	3644.1	8.4	1
2459026.95427	3664.0	13.2	4
2459026.95427	3720.5	8.8	5
2459027.88275	3644.1	9.3	1
2459027.88275	3674.3	12.7	4
2459027.88275	3711.1	9.1	5
2459027.92549	3639.9	8.7	1
2459027.92549	3705.3	9.0	5
2459027.92549	3708.8	12.7	4
2459059.90505	3650.7	33.1	1
2459059.90505	3661.4	17.2	5
2459059.90505	3705.6	15.1	4
2459059.93701	3608.4	19.3	1
2459059.93701	3673.9	15.8	4
2459059.93701	3730.6	22.3	5
2459061.88858	3635.0	18.9	1
2459061.88858	3692.4	67.1	4
2459061.88858	3716.7	16.3	5
2459061.92055	3671.7	51.9	1
2459061.92055	3677.5	20.8	5
2459062.88413	3659.1	58.8	1
2459062.88413	3683.6	15.9	4
2459062.88413	3715.9	23.8	5
2459062.91608	3696.2	17.9	1
2459062.91608	3731.7	16.0	4
2459062.91608	3796.8	32.4	5
2459064.89018	3676.3	26.6	1
2459064.89018	3736.8	15.2	4
2459064.89018	3742.1	17.3	5
NRES			
2459021.21141522	3398.2	17.7	SAAO
2459036.23065811	3352.7	13.1	SAAO
2459047.21646529	3392.2	14.2	SAAO
2459046.25208904	3322.8	13.1	SAAO
2459053.22874907	3412.1	14.0	SAAO
2459008.29685002	3492.6	26.1	Wise
2459013.35257704	3287.8	36.3	Wise
2459023.27975045	3288.4	18.4	Wise
2459025.32730386	3244.6	28.4	Wise
2459038.28150024	3212.0	17.9	Wise
2459035.27860615	3207.5	22.6	Wise
2459041.2807924	3109.9	36.6	Wise

Table 2
Stellar Parameters for TOI-1842

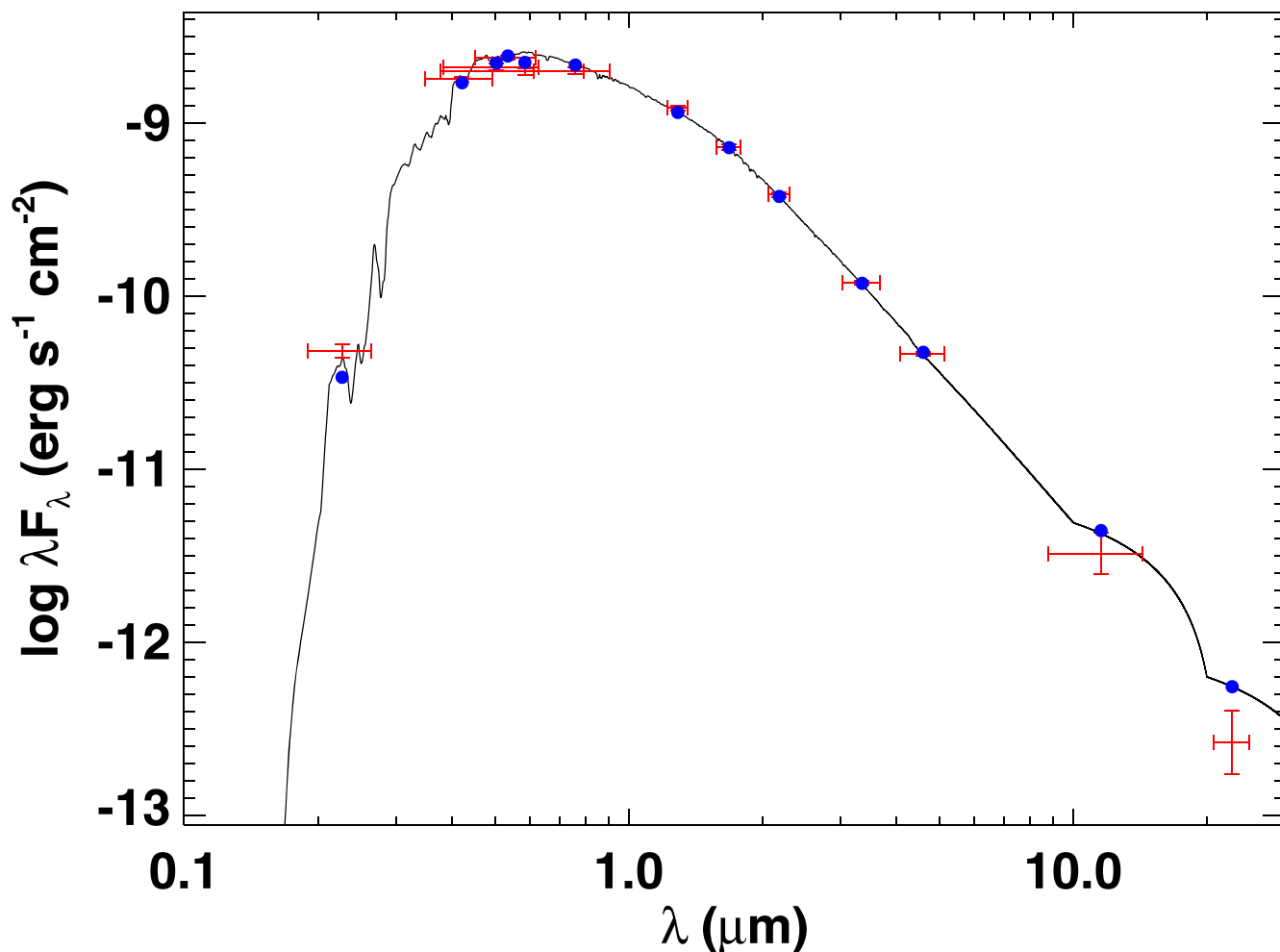| Parameter	Value	Reference
R.A. (h:m:s)	13:27:51.04	1
decl. (d:m:s)	+09:01:50.32	1
Distance (pc)	223.47 ± 2.24	1
V (mag)	9.81 ± 0.03	2
T (mag)	9.2673 ± 0.0061	3
T_{eff} (K)	6115 ± 119	3
	6239 ± 50	4
	6230 ± 50	5
$\log g$ (cm s^{-2})	3.876 ± 0.080	3
	4.25 ± 0.10	4
	4.10 ± 0.10	5
$R_\star$ ($R_\odot$)	2.05 ± 0.09	3
	2.02 ± 0.05	5
	2.013 ± 0.045	6
$L_\star$ ($L_\odot$)	5.29 ± 0.22	3
	5.50 ± 0.31	5
$M_\star$ ($M_\odot$)	1.15 ± 0.15	3
	1.46 ± 0.03	5
	1.78 ± 0.42	6
Metallicity, [M/H]	0.39 ± 0.08	4
	0.22 ± 0.05	5
Age (Gyr)	2.49 ± 0.22	5
$\rho_\star$ (g cm^{-3})	0.189 ± 0.041	3
	0.237 ± 0.021	6
	0.25 ± 0.02	5
$v \sin i$ (km s^{-1})	4.23 ± 0.20	5
	7.6 ± 0.5	4

Notes. Adopted values are shown in bold.
References. 1. Gaia Collaboration (2018); 2. Høg et al. (2000); 3. Stassun et al. (2019); 4. FIES spectrum (this work); 5. MINERVA-Australis spectrum (this work); 6. SED fit (Section 3.2).

(Addison et al. 2019). Each telescope simultaneously feeds stellar light via fiber optic cables to a single KiwiSpec R4-100 high-resolution ($R = 80,000$) spectrograph (Barnes et al. 2012) with wavelength coverage from 480 to 620 nm. Wavelength calibration is achieved with a simultaneous Th-Ar arc lamp observation through a calibration fiber. We obtained a total of 119 individual spectra from 2020 May 12 to 2020 Aug 3, with exposure times of 45–60 minutes, distributed among the three then-operational MINERVA-Australis telescopes as follows: T1—31; T4—42; T5—46. Radial velocities (Table 1) were derived for each telescope by cross correlation, where the template being matched is the mean spectrum of each telescope. The radial-velocity data suggested that the true orbital period is one-half of the period that had been initially reported by the TESS team. This finding was contemporaneously verified by TFOP SG1 photometry as described above.

2.2.2. LCOGT/NRES

We obtained 12 spectra of TOI-1842 using the Network of Robotic Echelle Spectrographs (NRES; Siverd et al. 2018) on

Addison et al. 2019, 2021). MINERVA-Australis consists of an array of four independently operated 0.7 m CDK700 telescopes situated at the Mount Kent Observatory in Queensland, Australia

Figure 1. Spectral energy distribution of TOI 1842. Red symbols represent the observed photometric measurements, where the horizontal bars represent the effective width of the passband. Blue symbols are the model fluxes from the best-fit Kurucz atmosphere model (black).

the LCOGT (Brown et al. 2013) telescope network. NRES is a set of four identical echelle spectograph units at observatory sites around the world. NRES achieves a resolving power of $R \sim 53,000$ with continuous coverage over 3900–8600 Å. We reduced the data and measured radial velocities using the CERES pipeline (Brahm et al. 2017). We obtained the data between 2020 June 7 and July 22 UT. Five of the spectra were obtained with the NRES unit at the Southern African Astronomical Observatory, South Africa, and seven with the unit at Wise Observatory, Israel.

2.2.3. FIES

A single spectrum of TOI-1842 was obtained on the night of 2020 May 27 (UT) using the FIbre-fed Échelle Spectrograph (FIES; Telting et al. 2014) at the Nordic Optical Telescope (NOT; Djupvik & Andersen 2010). We observed with the high-resolution fiber, which offers a resolution of $R \sim 67,000$ and has continuous wavelength coverage from about 3760 to 8220 Å. The data were reduced following Buchhave et al. (2010).
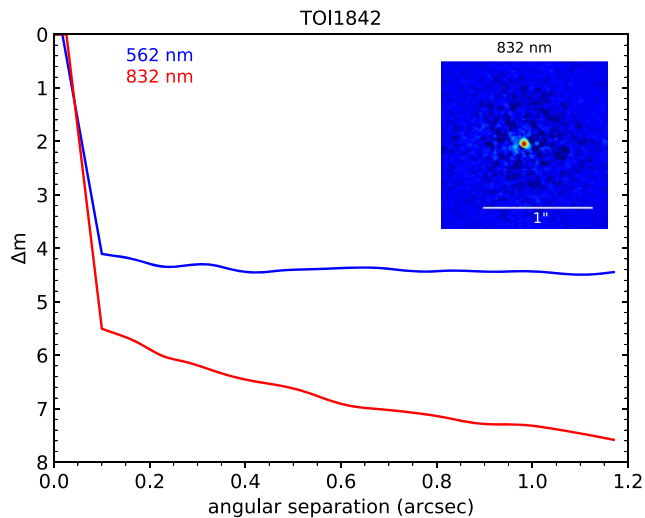
Figure 2. Zorro speckle observations of TOI-1842 obtained at 562 and 832 nm. The lines (red: 832 nm; blue: 562 nm) represent the 5σ contrast levels reached, revealing that no companion star is detected from the diffraction limit (17 mas) out to $1\farcs2$ within a Δ mag of 4 to 7.5. The inset shows the 832 nm reconstructed speckle image and has north up and East to the left.
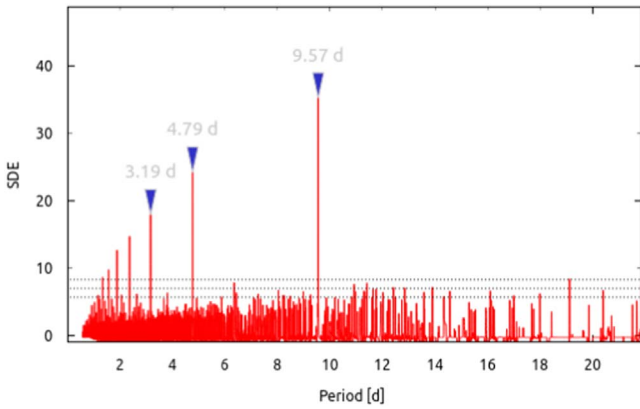
Figure 3. TLS power spectra of the detrended TESS PDCSAP light curve of Sector 23 and LCOGT data. Horizontal dashed lines indicates the signal detection efficiency power level of 5.7, 7.0, and 8.3, which corresponds to the TLS false-positive rate of 10%, 1%, and 0.1%. The strongest TLS power appears at 9.57 days, the remaining significant peaks are the low-frequency harmonics of the transit signal.

## 3. Stellar Properties of TOI-1842

3.1. Spectroscopic Stellar Parameter Determination

We derived stellar parameters for TOI-1842 using spectra from MINERVA-Australis as fully detailed in Addison et al. (2021). The spectroscopic parameters T_{eff}, $\log g$, and overall metallicity [M/H] were derived using iSpec (Blanco-Cuaresma et al. 2014; Blanco-Cuaresma 2019). Our derived T_{eff}, $\log g$, and [M/H] values were then used as input for the Bayesian isochrone modeler isochrones (Morton 2015; Montet et al. 2015) that uses the Dartmouth Stellar Evolution Database (Dotter et al. 2008). The isochrones modeling also included Gaia G, G_{BP}, G_{RP} magnitudes; 2MASS J, H, and K_S magnitudes along with Gaia EDR3 parallax values and their respective errors.

The extracted FIES spectrum was compared to a library of synthetic templates to measure effective temperature T_{eff}, surface gravity $\log g$, projected rotational velocity $v \sin i$, and metallicity [M/H] (a solar mix of metals, rather than Fe only). Our analysis follows Buchhave et al. (2012) and Buchhave et al. (2014), using five spectral orders spanning a wavelength range from 5065 to 5320 Å.

The spectroscopic and derived physical parameters for TOI-1842 are given in Table 2. In summary, we find that TOI-1842 is a slightly evolved subgiant star which is somewhat more massive and metal-rich than the Sun. While the stellar mass from the TIC is 2σ different from that derived with the Minerva-Australis spectrum, we note that the TIC mass does not use a spectroscopic $\log g$, which can lead to discrepancies in derived masses (e.g., Clark et al. 2021). The isochrones-derived stellar mass and radius are adopted for the joint modeling as presented in the next section.

3.2. Spectral Energy Distribution

In order to provide an initial empirical constraint on the stellar radius and mass, we performed an analysis of the broadband spectral energy distribution (SED) together with the Gaia DR2 parallax following the procedures described in Stassun & Torres (2016) and Stassun et al. (2017, 2018). We used the NUV flux from GALEX, the $B_T V_T$ magnitudes from Tycho-2, the JHK_S magnitudes from 2MASS, the W1–W4 magnitudes from WISE, and the $GG_{BP}G_{RP}$ magnitudes from Gaia. Together, the available
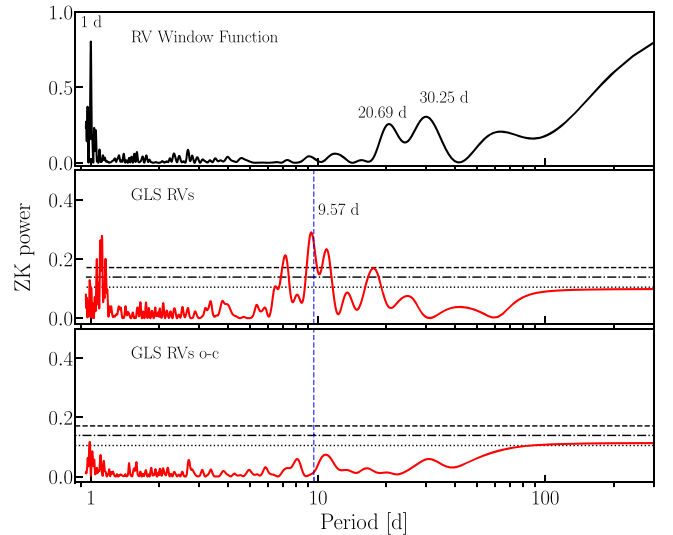
Figure 4. Top panel: window function power spectrum of the combined Doppler data for TOI-1842. Middle panel: GLS power spectra of the Doppler data of TOI-1842. Horizontal dashed lines indicate GLS false-positive thresholds of 10%, 1%, and 0.1%. A significant periodic signal is detected at a period of 9.34 days, which is induced by TOI-1842b. The other significant signals near ~10.8, 7.10, and 1.12 days are aliases of the window function and the planetary signal. Bottom panel: same as above panel, but for the RV residuals of the best joint model of TOI-1842.

photometry spans the full stellar SED over the wavelength range 0.2–22 μm (see Figure 1).

We performed a fit using Kurucz stellar atmosphere models, adopting the effective temperature (T_{eff}), surface gravity ($\log g$), and metallicity ([Fe/H]) from the spectroscopically determined values. The extinction (A_V) was allowed to vary but limited to the maximum line-of-sight extinction from the dust maps of Schlegel et al. (1998). The resulting fit is very good (Figure 1) with a reduced χ^2 of 1.4. Integrating the (unreddened) model SED gives the bolometric flux at Earth of $F_{bol} = 3.278 \pm 0.076 \times 10^{-9}$ erg s^{-1} cm^{-2}. Taking the F_{bol} and T_{eff} together with the Gaia DR2 parallax, adjusted by $+0.08$ mas to account for the systematic offset reported by Stassun & Torres (2018), gives the stellar radius as $R_\star = 2.013 \pm 0.045\ R_\odot$.

In addition, we can compute an empirical estimate for the stellar mass via the empirical stellar radius above together with the spectroscopic $\log g$, which gives $M_\star = 1.8 \pm 0.4\ M_\odot$, consistent with the empirical eclipsing-binary-based relations of Torres et al. (2010), which give $M = 1.37 \pm 0.08\ M_\odot$. The mass and radius together give a mean stellar density of $\rho_\star = 0.24 \pm 0.02$ g cm^{-3}. These estimates are also consistent with the mass and radius derived from the MINERVA-Australis spectra.

Finally, from the spectroscopic $v \sin i$ and the stellar radius we obtain an upper limit on the stellar rotation period, $P_{rot} / \sin i = 13.4 \pm 0.9$ days. Using the empirical gyrochronology relations of Mamajek & Hillenbrand (2008), this then provides upper limits on the stellar age of ≈ 1.9 Gyr (1σ) and ≈ 1.5 Gyr (3σ). The lack of lithium absorption in the FIES spectrum also places a lower age limit of ~800 Myr.

3.3. High-resolution Imaging

We observed TOI-1842 with optical speckle interferometric imaging as part of our standard process for validating transiting exoplanets to assess the possible contamination of bound or

Table 3
Nested Sampling Posteriors and Maximum $-\ln \mathcal{L}$ of the Orbital and Nuisance Parameters of the TOI-1842 System

Parameter	Median and 1σ	Max. $-\ln \mathcal{L}$	Adopted Priors
K [m s^{-1}]	$15.9^{+2.9}_{-2.80}$	16.8	$\mathcal{U}(5.0,30.00)$
P [day]	$9.5739^{+0.0002}_{-0.0001}$	9.5739	$\mathcal{U}(9.565,9.580)$
t_0 [deg]	$2459402.4575^{+0.0026}_{-0.0024}$	2459402.4572	$\mathcal{U}(2459402.2,2459402.6)$
i [deg]	$88.4^{+0.9}_{-1.5}$	88.3	$\mathcal{U}(80.0,90.0)$
$a/R_\star$	$16.2^{+1.6}_{-2.9}$	16.1	$\mathcal{U}(5.0,15.00)$
$R/R_\star$	$0.052^{+0.003}_{-0.002}$	0.052	$\mathcal{U}(0.01,0.10)$
a [au]	$0.1001^{+0.0007}_{-0.0007}$	0.0925	(derived)
m_p [$M_{\rm jup}$]	$0.214^{+0.040}_{-0.038}$	0.225	(derived)
R_p [$R_{\rm jup}$]	$1.04^{+0.06}_{-0.05}$	1.05	(derived)
RV off.$_{\rm MINERVA\ TEL\ 1}$ [m s^{-1}]	$3603.0^{+11.2}_{-11.6}$	3595.3	$\mathcal{U}(3200,3800)$
RV off.$_{\rm MINERVA\ TEL\ 4}$ [m s^{-1}]	$3652.5^{+10.8}_{-11.4}$	3646.0	$\mathcal{U}(3200,3800)$
RV off.$_{\rm MINERVA\ TEL\ 5}$ [m s^{-1}]	$3665.9^{+9.9}_{-10.5}$	3659.3	$\mathcal{U}(3200,3800)$
RV off.$_{\rm NRES}$ [m s^{-1}]	$3337.5^{+34.9}_{-28.3}$	3332.9	$\mathcal{U}(3200,3800)$
RV jitter$_{\rm MINERVA\ TEL\ 1}$ [m s^{-1}]	$15.2^{+3.9}_{-4.6}$	15.7	$\mathcal{J}(1.00,25.00)$
RV jitter$_{\rm MINERVA\ TEL\ 4}$ [m s^{-1}]	$18.7^{+3.4}_{-5.8}$	17.5	$\mathcal{J}(1.00,25.00)$
RV jitter$_{\rm MINERVA\ TEL\ 5}$ [m s^{-1}]	$9.5^{+3.3}_{-3.5}$	8.8	$\mathcal{J}(1.00,25.00)$
RV jitter$_{\rm NRES}$ [m s^{-1}]	$43.2^{+22.1}_{-16.6}$	45.4	$\mathcal{J}(1.00,100.00)$
RV lin. trend [m s^{-1}/day]	$0.316^{+0.254}_{-0.121}$	0.395	$\mathcal{J}(-5.00,5.00)$
Transit offset$_{\rm TESS-S21}$ [ppm]	46^{+8}_{-8}	45	$\mathcal{N}(0.0,1000.0)$
Transit offset$_{\rm LCO-SAAO}$ [ppm]	11^{+110}_{-108}	-5	$\mathcal{N}(0.0,1000.0)$
Transit offset$_{\rm LCO-CTIO\ 1}$ [ppm]	158^{+140}_{-127}	118	$\mathcal{N}(0.0,1000.0)$
Transit offset$_{\rm LCO-CTIO\ 2}$ [ppm]	-1834^{+132}_{-122}	-1811	$\mathcal{N}(0.0,1000.0)$
Transit jitter$_{\rm TESS-S21}$ [ppm]	40^{+50}_{-23}	22	$\mathcal{J}(0.0,1000.0)$
Transit jitter$_{\rm LCO-SAAO}$ [ppm]	1143^{+94}_{-82}	1127	$\mathcal{J}(0.0,1000.0)$
Transit jitter$_{\rm LCO-CTIO\ 1}$ [ppm]	1275^{+123}_{-85}	1277	$\mathcal{J}(0.0,1000.0)$
Transit jitter$_{\rm LCO-CTIO\ 2}$ [ppm]	1638^{+120}_{-85}	1635	$\mathcal{J}(0.0,1000.0)$
Quad. limb-dark.$_{\rm TESS}$ u_1	$0.307^{+0.235}_{-0.175}$	0.151	$\mathcal{U}(0.00,1.00)$
Quad. limb-dark.$_{\rm TESS}$ u_2	$0.586^{+0.255}_{-0.315}$	0.718	$\mathcal{U}(0.00,1.00)$
Quad. limb-dark.$_{\rm LCO}$ u_1	$0.327^{+0.226}_{-0.190}$	0.292	$\mathcal{U}(0.00,1.00)$
Quad. limb-dark.$_{\rm LCO}$ u_2	$0.481^{+0.293}_{-0.291}$	0.508	$\mathcal{U}(0.00,1.00)$

unbound companions on the derived planetary radii (Ciardi et al. 2015). Speckle imaging observations of TOI-1842 were performed on 2021 March 1 UT using the Zorro speckle instrument on Gemini-South.[32] Zorro simultaneously provides speckle imaging in two bands, 562 and 832 nm, with output data products including a reconstructed image, and robust limits on companion detections (Howell et al. 2011). Figure 2 shows our results for TOI-1842 from both bandpasses and the reconstructed 832 nm speckle image. We find that TOI-1842 is indeed a single star with no detected companion brighter than $\Delta_{\rm mag} \sim 4$–7.5 magnitudes (M0V) detected within $1\rlap{.}''2$. The angular resolution limits of the speckle observations, at the distance of TOI-1842 ($d = 223.5$ pc), correspond to spatial limits of 4.5 to 268 au.

4. Analysis and Results

We used the `Exo-Striker` exoplanet toolbox[33] (Trifonov 2019) to perform a signal analysis and a joint fit of the transit light curve and radial-velocity data. For the photometric transit period search, `Exo-Striker` uses the `transitleastsquares` package (TLS; Hippke & Heller 2019), and for the RV-period search analysis, it uses the generalized
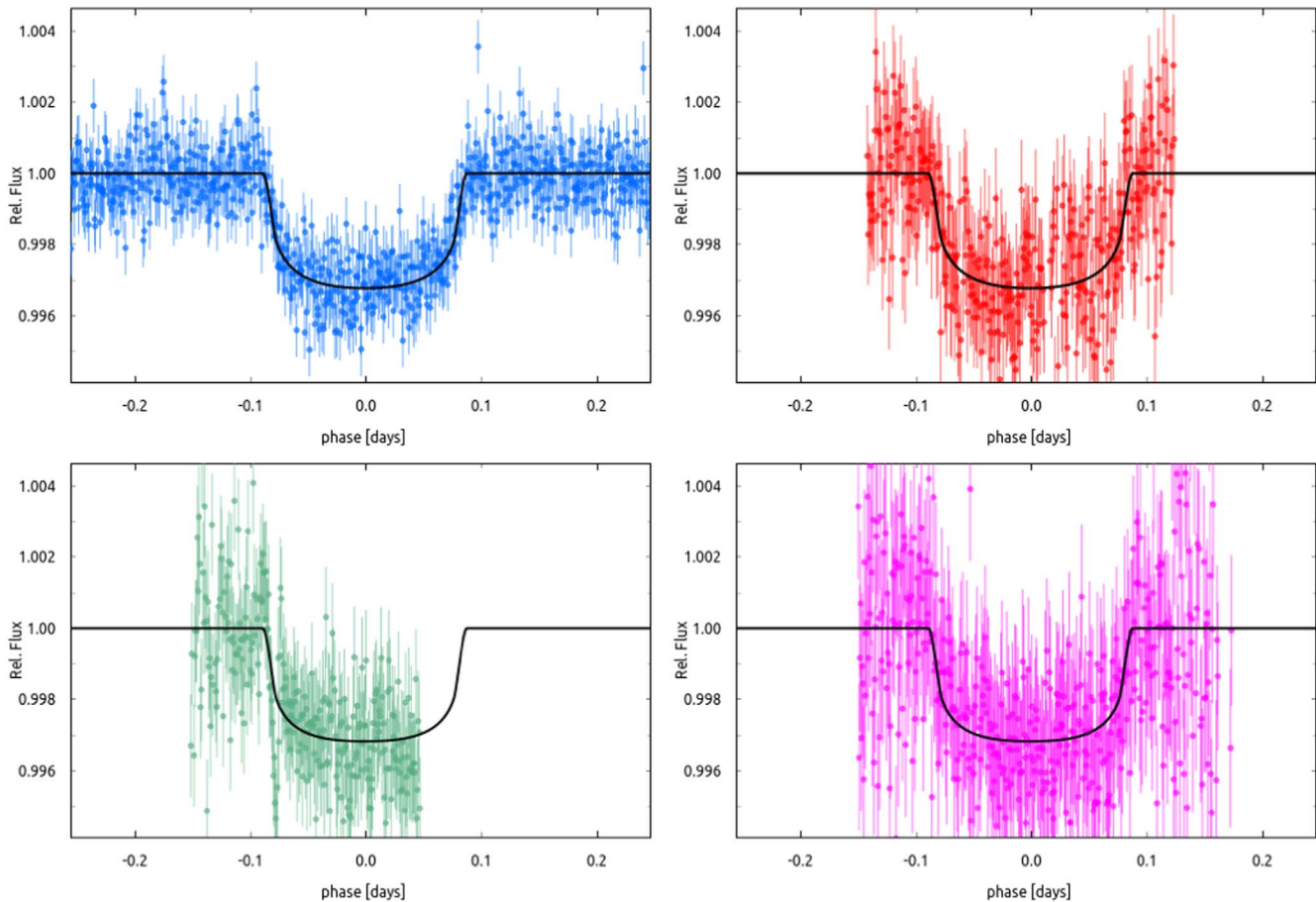
Lomb–Scargle periodogram (GLS; Zechmeister & Kürster 2009). `Exo-Striker` allows for wide variety of joint-modeling schemes of multitelescope transit and RV data consistent with planetary signals. The modeling can be performed either by "best-fit" optimization schemes (i.e., Levenberg-Marquardt, Nelder-Mead, Newton, etc.), or sampling schemes such as an affine-invariant ensemble Markov chain Monte Carlo sampler (Goodman & Weare 2010) via the `emcee` package (Foreman-Mackey et al. 2013), and the nested sampling technique (Skilling 2004) via `dynesty` sampler (Speagle 2020), which allow detailed posterior probability analysis.

4.1. Signal Search

Figure 3 shows the TLS signal detection efficiency power spectra of the detrended relative flux of the TESS and the LCOGT data of TOI-1842. We detect a significant transit event on the combined light-curve data with a period of 9.5742 ± 0.0024 days, $t_0 = 2458933.32187$, a mean transit duration of 4.272 hr, and a mean transit depth of 0.9967 in relative flux units. Figure 3 also shows that TLS detects other significant periodicities in the data, which, however, are attributed to the 1/2, 1/3, 1/4, etc, low-frequency harmonics of the actual transit period. Our independent transit-search analyses are in agreement with the available SPOC DV estimates based on the TESS Sector 23 data of TOI-1842.

---

[32] https://www.gemini.edu/sciops/instruments/alopeke-zorro/
[33] https://github.com/3fon3fonov/exostriker

Figure 5. Transit photometry data and model fit for TESS (blue, Sector 23), LCOGT data from SAAO (red), and CTIO (green and magenta). The transit model (black solid line) is constructed jointly with precise Doppler data as described in Section 4.2.

Figure 4 shows the period search analysis of the combined MINERVA-Australis and NRES RV data set. The top panel of Figure 4 shows the window function of the available Doppler data of TOI-1842. The observational scheduling results in strong window function power at periods of 1, 20.54, 29.98 days, and lower frequencies. The middle panel of Figure 4 shows the GLS power spectra of the Doppler data of TOI-1842. Horizontal dashed lines indicate GLS false-positive thresholds of 10%, 1%, and 0.1%. We detect a significant periodic signal with a period of 9.34 ± 0.15 days, which is near the period of the transit signal. The remaining significant signals are aliases of the window function and the Doppler-induced planetary signal. The bottom panel of Figure 4 shows the GLS power spectrum of the RV residuals of the joint fit (see Section 4.2). We did not detect any significant residual RV periodicity suggesting the presence of any additional planet.

4.2. Combined Transit and RV-orbital Analysis

We use the TLS and GLS results from Section 4.1 as a starting point for our combined transit and RV-orbital modeling. From these estimates and the following intermediate transit and RV parameter optimization analysis with the Exo-Striker, we define informative and noninformative parameter priors needed for our global parameter search. We performed multidimensional parameter fitting, constructing the posterior probability distribution by employing a nested sampling scheme using the dynesty sampler. We set 100 "live points" per fitted parameter, sampled via random walk,

dynamic nested sampling with a 100% weight on the posterior convergence (see Speagle 2020 for details). Our adopted dynamic nested sampling scheme allows us to construct a posterior probability distribution, from which we adopted the 68.3 % confidence levels as 1σ parameter uncertainties. In addition, the nested sampling analysis is very convenient for an adequate model comparison via the difference of their Bayesian log-evidence $\Delta \ln Z$.[34] Our adopted parameter priors, the resulting median values and their 1σ uncertainties drawn from the posterior probability distribution, and the sample with the maximum $-\ln \mathcal{L}$ (i.e., best-fit) for our final orbital analysis are summarized in Table 3. Figure 5 shows the best-fit transit model component applied to Sector 21 and the LCOGT data, whereas Figure 6 shows the RV component of the joint-fit model applied to the combined RVs. Our combined transit and RV-orbital analyses are performed as follows.

The transit modeling within the Exo-Striker is done by a wrapper of the BAsic Transit Model cAlculatioN package (batman; Kreidberg 2015). This package constructs the transit light-curve model by accepting planetary orbital parameters such as period P, eccentricity e, the argument of periastron, ω, and inclination i, which are common to the Keplerian RV model of the Exo-Striker. Additional transit parameters of batman are the time of inferior transit conjunction t_0, and the

---

[34] $\Delta \ln Z = \ln Z_{\text{complex model}} - \ln Z_{\text{simpler model}}$. Two models are indistinguishable if their Bayesian log-evidence difference satisfies $\Delta \ln Z \lesssim 2$, a model moderately favored over another if $\Delta \ln Z > 2$, and strongly favored if $\Delta \ln Z > 5$ (Trotta 2008).
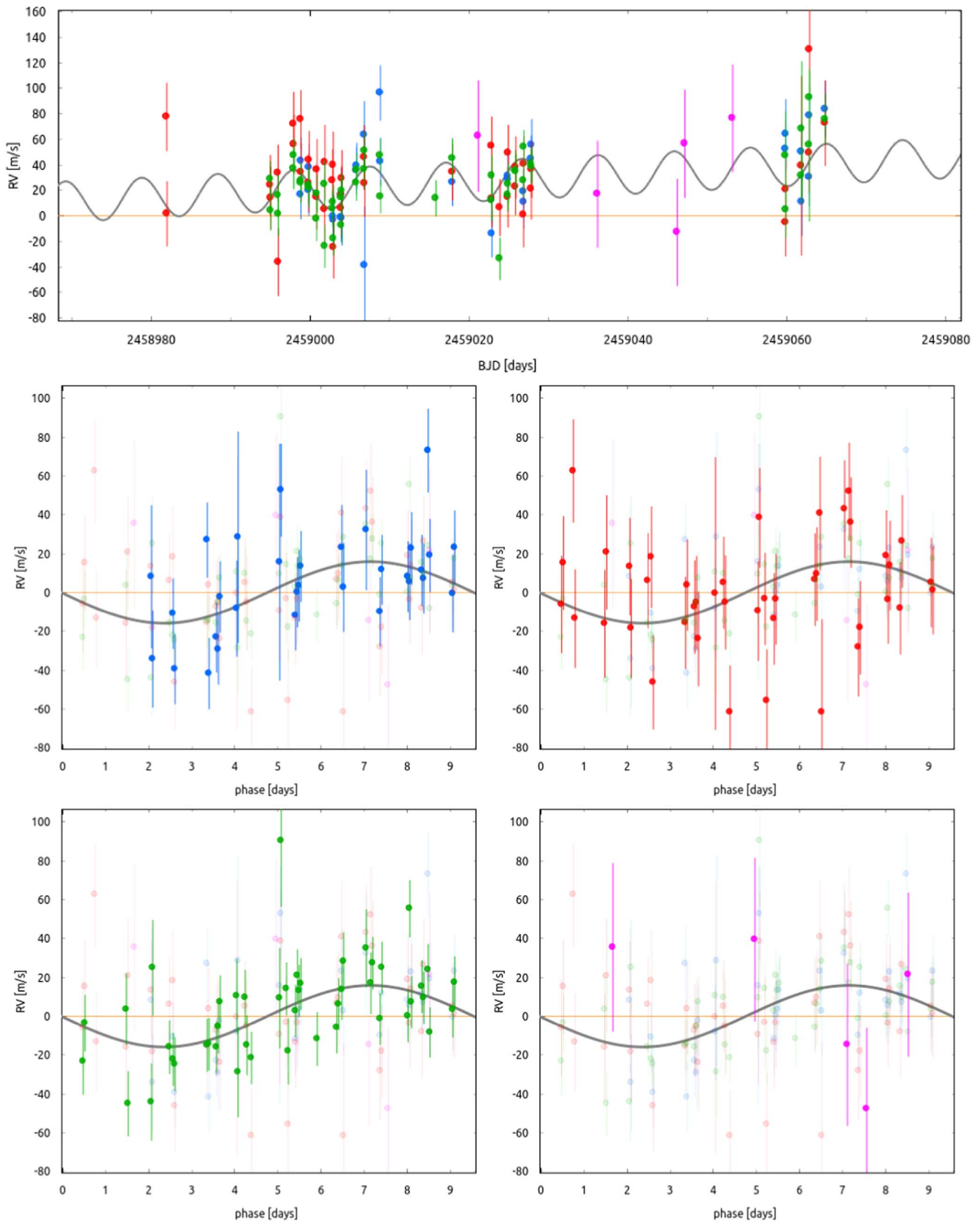
Figure 6. Radial-velocity data and model fit for TOI-1842. Top: complete time series and joint fit model including a linear trend. Bottom: phase-folded RV data, with each of the four instruments individually highlighted (with heavier points) in each subpanel for clarity. Left to right subpanels: MINERVA-Australis Telescopes 1 (blue), 4 (red), 5 (green), and NRES/SAAO (purple).
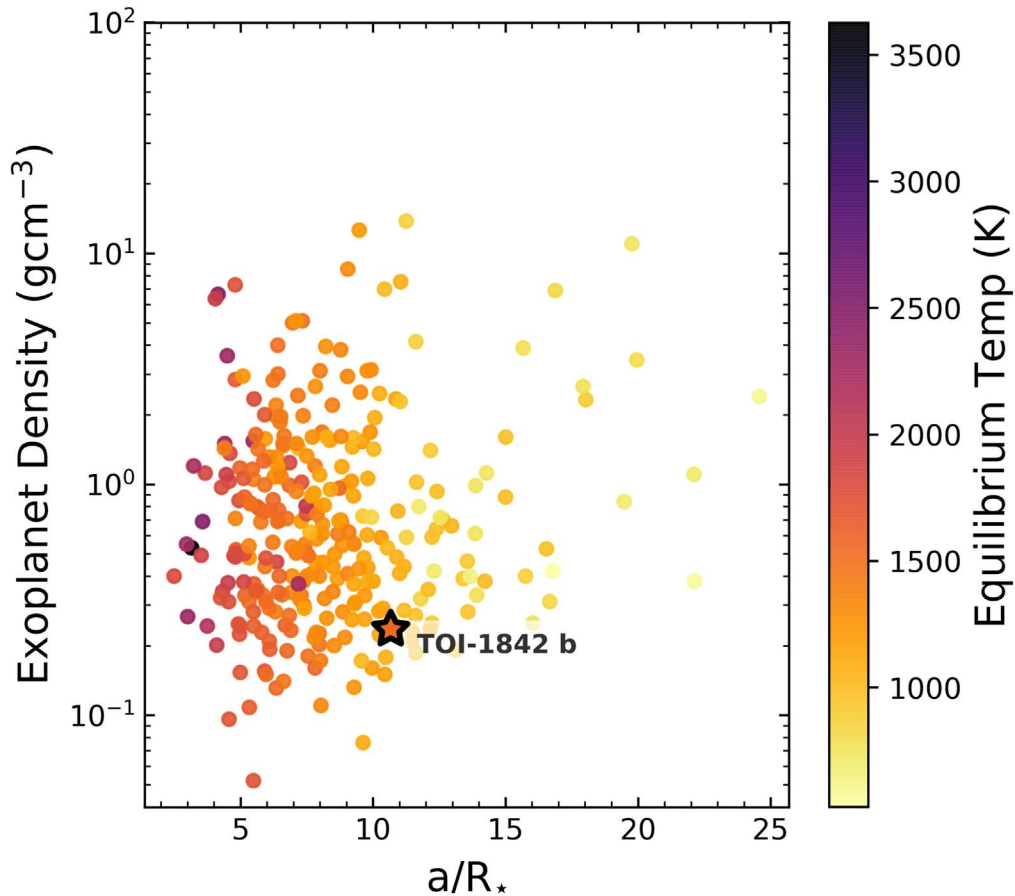
Figure 7. Planetary density as a function of orbital distance $a/R_\star$ for 410 hot Jupiters. Only 37 hot Jupiters have bulk densities smaller than TOI-1842b (starred in this plot).

planet semimajor axis and radius in units relative to the stellar radius $a/R_\star$ and $R/R_\star$, respectively. The RV model component fits the RV signal semiamplitude K, which constrains the planetary mass.

In addition to the orbital parameters, our modeling scheme includes a number of nuisance parameters, which we optimize simultaneously. For each transit and RV data set we fit their respective relative mean offset and additional data "jitter" terms, the latter of which was simultaneously added in quadrature to the data error budget while evaluating the models' (negative) log-likelihood $-\ln\mathcal{L}$ (Baluev 2009). In particular, we model the light curve of TESS obtained in Sector 21 and the LCOGT data of SAAO, CTIO 1, and CTIO 2, which adds eight additional parameters. We adopt separate quadratic limb-darkening transit models of TESS and LCOGT, for which we optimize separate quadratic limb-darkening coefficients, $u1_{\mathrm{TESS}}$ and $u2_{\mathrm{TESS}}$, and $u1_{\mathrm{LCOGT}}$ and $u2_{\mathrm{LCOGT}}$, respectively. For the RV data, we fit the precise RVs of MINERVA obtained with telescopes 1, 4, and 5 and the NRES-CPT, which also adds eight nuisance parameters. We do not include the NRES-Wise RVs in our joint fit since we found that their scatter is too large, and overall, does not improve the outcome of our analysis. In addition, we find a marginally significant positive Doppler drift in the combined RV data, which is possibly induced by another companion orbiting at a greater distance. No companions are visible (Figure 2), and there is only one object within 1 arcmin, a faint background star at $T = 17.595$,

separated by $28''$. Since the nature of this signal cannot be determined based on the available data, we model it by applying an additional RV linear trend parameter.

We performed two sets of joint-fit nested sampling analysis: for a forced circular orbit of TOI-1842b ($e = 0$, for which ω is undefined), and with free e and ω. We found that the simpler circular model is moderately favored with a log evidence of $\ln Z = 82096.06$, whereas the full-Keplerian model has a slightly poorer log-evidence of $\ln Z = 82093.65$. From the full-Keplerian model, we find that the orbital eccentricity is consistent with 0, but with large uncertainties, from which we estimate an upper eccentricity limit of $e < 0.25$ at the 1σ level. Thus, as a final orbital solution of TOI-1842b, we adopted the simpler, circular orbit joint-fit model, which is presented in Table 3, as well as Figures 5 and 6.

The values of three most representative parameters from our best fit are $P = 9.5739^{+0.0002}_{-0.0001}$ days, $t_0 = 2459402.4575^{+0.0026}_{-0.0024}$ days, and $K = 15.9^{+2.9}_{-2.80}$ m s^{-1}. Given the parameter posteriors, and our estimates of the stellar mass, radius, and their uncertainties, we derive a dynamical planetary mass of $m_{\mathrm{pl.}} = 0.214^{+0.040}_{-0.038} M_{\mathrm{Jup}}$, semimajor axis of $a = 0.1001^{+0.0007}_{-0.0007}$ au, and a planetary radius of $R_{\mathrm{pl.}} = 1.04^{+0.06}_{-0.05} R_{\mathrm{Jup}}$, which makes it one of the lowest-density planets discovered to date ($\rho = 0.252 \pm 0.091$ g cm^{-3}).

We further inspected the TESS residuals with TLS and the RV residuals with GLS to check for evidence of additional planets, but none was found.
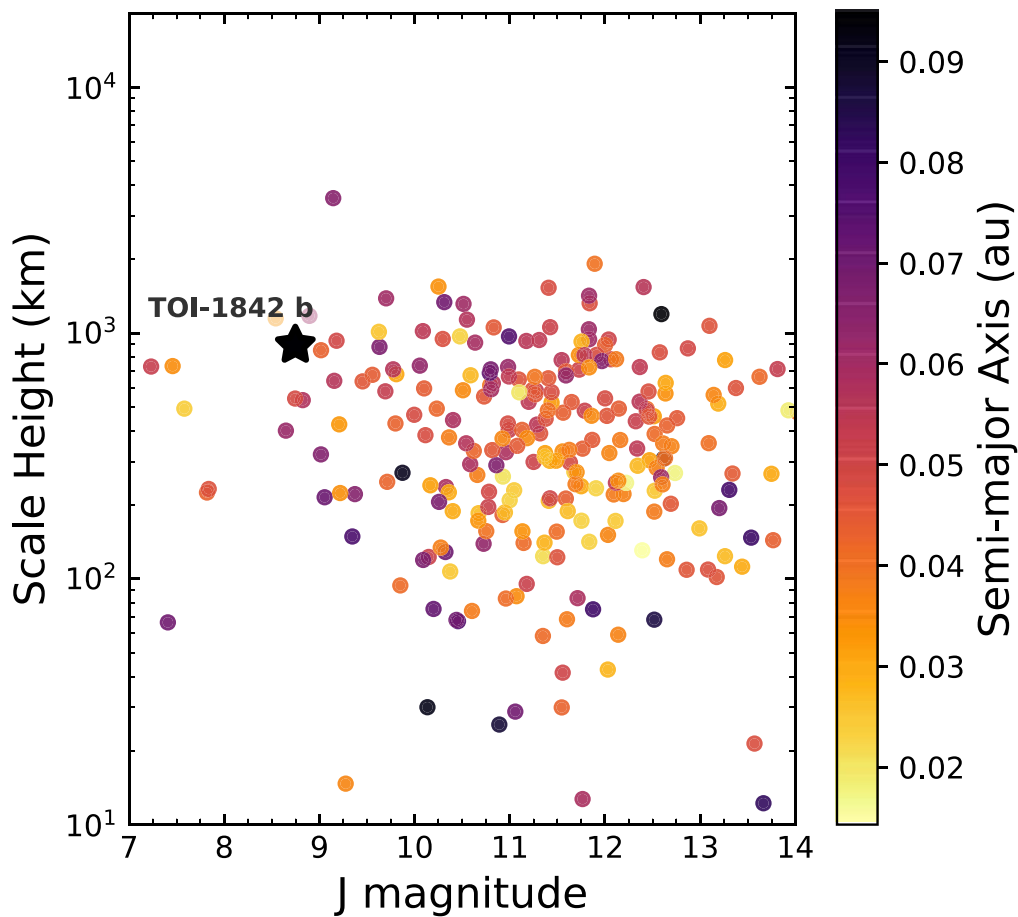
Figure 8. Estimated atmospheric scale height vs. J magnitude for 410 giant planets ($R_p > 0.75\ R_J$). With a scale height of 893 km, TOI-1842b is an attractive target for atmospheric characterization. Only WASP-76b (West et al. 2016) presents a larger scale height and a brighter host star.
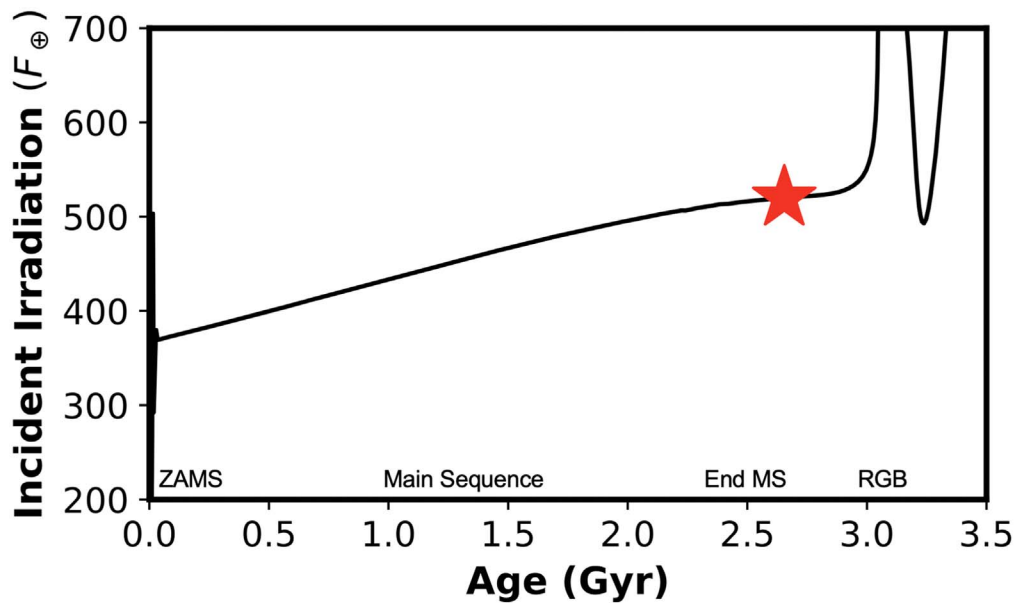

Figure 9. Incident irradiation received by TOI-1842b over the course of the host star evolution. Assuming no tidal modification of the orbit of the planet, TOI-1842b is now receiving 30% more incident irradiation ($\sim$550 $F_\oplus$) than it did when the host star settled on the main sequence.

5. Discussion and Conclusions

We have confirmed the planetary nature of the warm Saturn TOI-1842b ($P = 9.5737 \pm 0.0015$ days), and we have measured its mass to be $0.214^{+0.040}_{-0.038}\ M_J$, with a radius of $1.04^{+0.06}_{-0.05}\ R_J$. This

planet, moving on a circular orbit with $a = 0.10$ au about its subgiant host star, joins a small cohort of 56 confirmed planets orbiting within 0.5 au of evolved stars. With a period of nearly 10 days, this planet's orbital properties are similar to TOI-481b
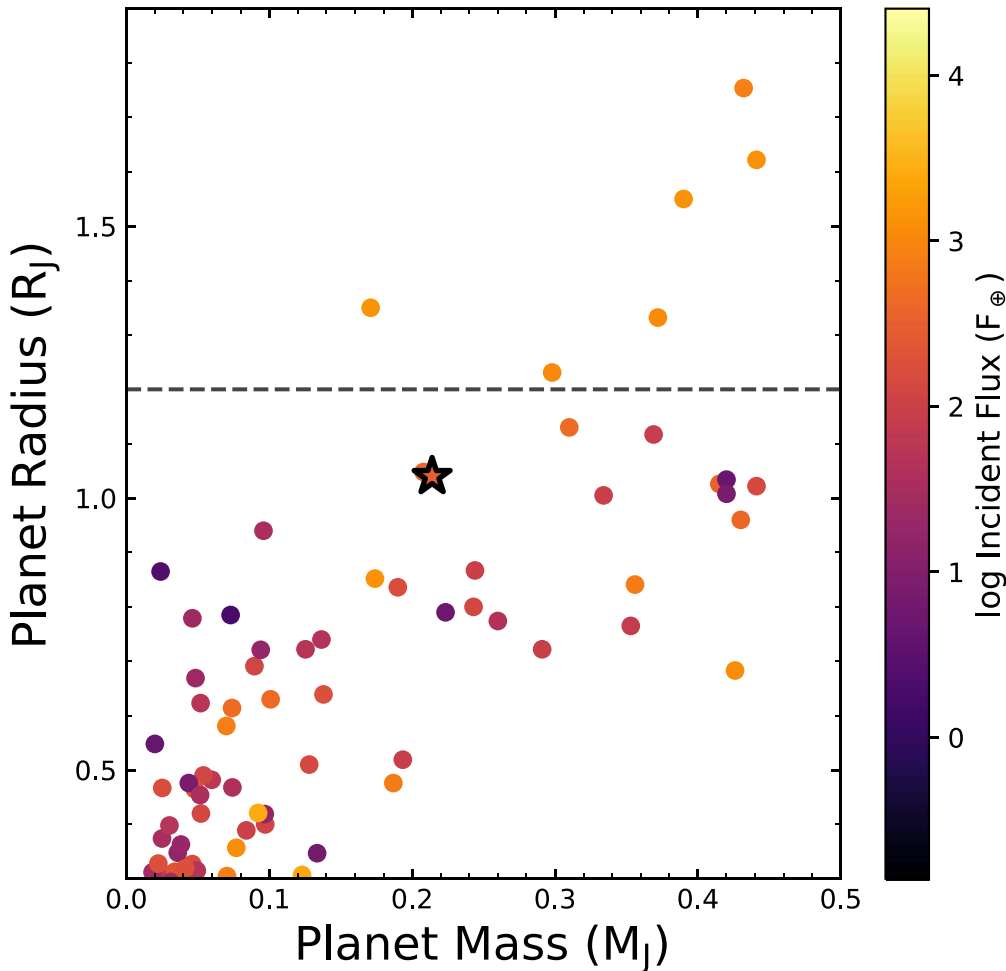
Figure 10. Planet radius vs. mass (in Jupiter units) for well-characterized Saturns, color coded by incident flux in terms of the flux received by Earth ($F_\oplus$). TOI-1842b is marked as a large star. The dashed line at 1.2 R_J denotes the approximate maximum radius for uninflated planets, as given by Lopez & Fortney (2016).

(Brahm et al. 2020), another warm giant ($T_{eq} = 1210 \pm 29$ K) orbiting a slightly evolved metal-rich star. While short-period giant planets orbiting stars more massive than the Sun remain rare, such planets appear to be preferentially found around supersolar metallicity stars, as evidenced by the positive planet-metallicity correlation found for evolved stars by several studies (e.g., Reffert et al. 2015; Jones et al. 2016; Wittenmyer et al. 2020; Wolthoff 2021). Petigura et al. (2018) also found that warm Saturns in particular are intrinsically less common than close-in Neptunes or Jupiters, and tend to be hosted by metal-rich stars. The properties of TOI-1842b are thus consistent with this class of rare low-mass gas giants.

TOI-1842b is remarkable due to its low density ($\rho = 0.252 \pm 0.091$ g cm^{-3}), which ranks it among the least-dense 9.3% of known planets. Figure 7 places this planet in context of the cohort of planets with measured bulk densities. From the derived equilibrium temperature (1210 K) and surface gravity of the planet and assuming a H/He atmosphere with a mean molecular mass of $\mu = 2.3$ amu, the calculated atmospheric scale height (from $H_b = kT_{eq}/(\mu g_b)$) is $H_b = 893$ km.[35] The large scale height of TOI-1842b ($h/R_p = 1.2\%$) is reminiscent of KELT-11b (Figure 8). While KELT-11b has a larger scale height (Pepper et al. 2017), its primary transit time

of ~8 hr would require multiple full night observations to fully observe. Alternatively, TOI-1842b has a transit duration of ~4 hr, making it an ideal candidate for single night observation follow up. The transmission spectroscopy metric (TSM; Kempton et al. 2018), used to assess the suitability of transmission spectroscopy observations with the James Webb Space Telescope (JWST), for TOI-1842b is 141. Planets with TSM values greater than ~96 (for Jovians and sub-Jovians), such as for TOI-1842b, are considered suitable for these observations with JWST.

The measured mass and radius of TOI-1842b place it within the category of "inflated sub-Saturns." From the relationship given in Weiss et al. (2013), TOI-1842b has a predicted radius of 9 $R_\oplus$; its measured radius of 11.65 $R_\oplus$ is thus ~30% larger than a noninflated planet with its mass and incident flux. Inflated sub-Saturn planets occupy a relatively unexplored parameter space that is seen as a key transitional population group between inflated super-Earths and Jovian worlds (Lee & Chiang 2016; Colón et al. 2020). Conversely, the low density of some planets in longer period orbits, like TOI-1842b, might be indicative of their formation pathways. Lee & Chiang (2016) proposed that low density sub-Saturns formed in situ. The chemical composition of these planets should reflect the composition of the gas disk from which they were formed (Öberg et al. 2011). Furthermore, TOI-1842b is a rare close-in planet orbiting an evolved star. By observing and

---

[35] For comparison, Jupiter has the largest scale height in our Solar System at 27 km.
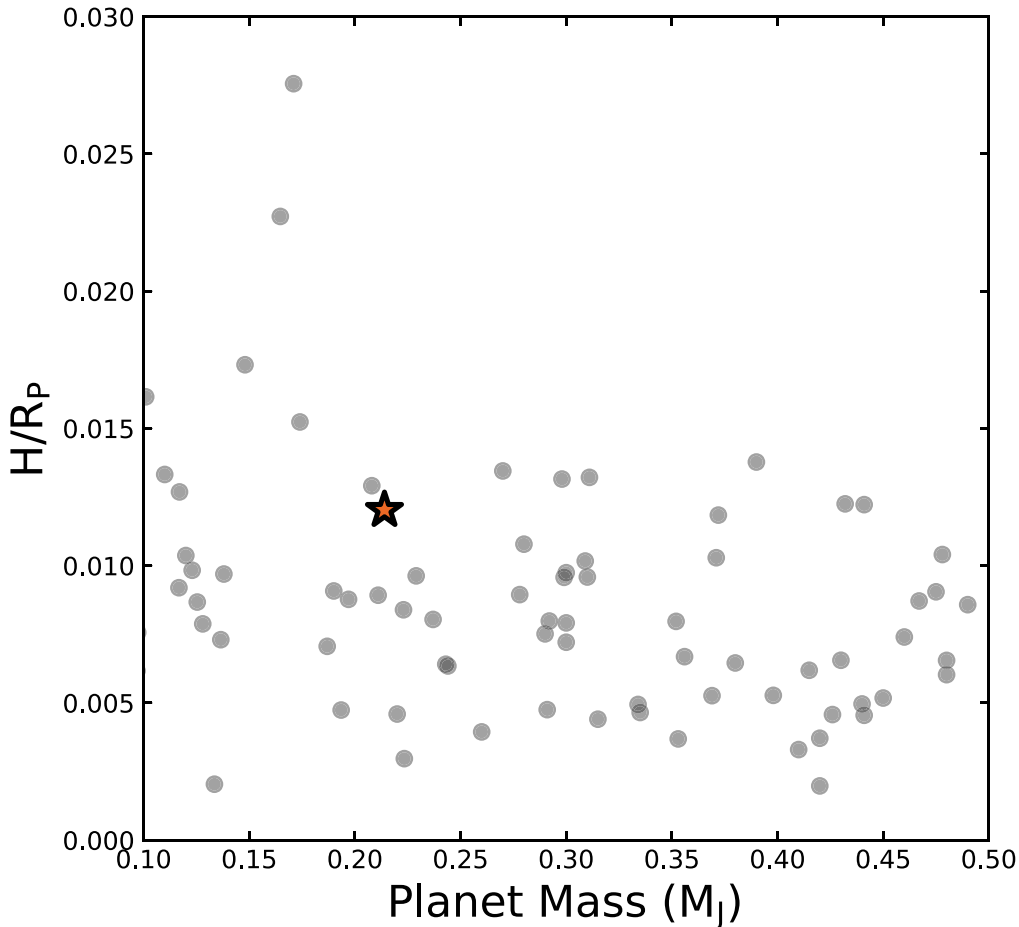
Figure 11. Relative atmospheric scale height (H/R_p) vs. planet mass for well-characterized Saturns. TOI-1842b is marked as a large star, and is among the most favorable targets in this mass regime.

identifying the molecular species and physical dynamics present within the atmosphere of TOI-1842b, we can obtain a better understanding on how these inflated gas giants interact with their host star over time and better determine the formation process for this population.

The radius and mass of TOI-1842b, at its orbital distance of 0.1 au, are consistent with a coreless planet (see Table 4 in Fortney et al. 2007). We note that the host star is metal-rich with nearly twice Solar [M/H], making the presence of a coreless giant planet most intriguing. One would expect metal-rich protoplanetary disks to form planets with larger solid cores due to a higher surface density (Pollack et al. 1996). For example, HD 149026 with a similar metal content hosts a planet with a $\sim$67 $M_\oplus$ core (Sato et al. 2005). TOI-1842b thus presents a fascinating conundrum; a relatively rare class of planet for which detailed atmospheric studies will be eminently feasible and illuminating.

TOI-1842b joins a growing list of low density close-in gas giants orbiting stars evolving off the main sequence (e.g., Wang et al. 2019; Bryant et al. 2020; Sha et al. 2021), and provides a suitable test to models that explain the higher-than-expected radii of these gas giants via reinflation mechanisms (e.g., Lopez & Fortney 2016; Komacek et al. 2020; Thorngren et al. 2021). Adopting the stellar parameters from Table 2 and evolution tracks from the MIST models (Dotter 2016), the current irradiation received by TOI-1842b is 30% more than it originally received at zero-age main sequence (Figure 9). A

number of similarly inflated warm Jovian planets have recently been found around post-main-sequence stars receiving many times their main-sequence incident irradiation (e.g., Grunblatt et al. 2016; Hartman et al. 2016; Grunblatt et al. 2017; Pepper et al. 2017).

Figure 10 places TOI-1842b in context with other well-characterized sub-Jovian planets with masses and radii measured to precisions of better than 20% and 10%, respectively. The radius of TOI-1842b is near the upper envelope of similar planets in this mass regime. TOI-1842 is beginning to leave the main sequence and, as shown in Figure 9, will irradiate and further inflate TOI-1842b over the next tens of Myr before eventually consuming the planet (Villaver et al. 2014). As the star evolves off the main sequence, the strengthening incident irradiation and star-planet tidal interactions may induce increased heating of the planet's core, potentially reinflating the low density gas giants. While TOI-1842b is not at present immensely inflated by comparison to planets of similar mass, it stands out in its suitability for atmospheric characterization. In addition to the brightness of the host star (see Figure 8), TOI-1842b has a high ratio of atmospheric scale height to planetary radius. Figure 11 shows the ratio of atmospheric scale height to planet radius (H/R_p) as a function of mass for the cohort of well-characterized sub-Jovian planets. TOI-1842b lies in the best 10% of these planets in terms of H/R_p. The two highest points in Figure 11 with $H/R_p > 0.02$ are KELT-11b

(Pepper et al. 2017) and WASP-127b (Lam et al. 2017). Those two extremely inflated planets both orbit subgiant stars, and represent possible futures for TOI-1842b as its host star inexorably ascends the subgiant branch.

ORCID iDs

Robert A. Wittenmyer ⓘ https://orcid.org/0000-0001-9957-9304
Jake T. Clark ⓘ https://orcid.org/0000-0003-3964-4658
Trifon Trifonov ⓘ https://orcid.org/0000-0002-0236-775X
Brett C. Addison ⓘ https://orcid.org/0000-0003-3216-0626
Duncan J. Wright ⓘ https://orcid.org/0000-0001-7294-5386
Keivan G. Stassun ⓘ https://orcid.org/0000-0002-3481-9052
Jonathan Horner ⓘ https://orcid.org/0000-0002-1160-7970
Nataliea Lowson ⓘ https://orcid.org/0000-0001-6508-5736
John Kielkopf ⓘ https://orcid.org/0000-0003-0497-2651
Stephen R. Kane ⓘ https://orcid.org/0000-0002-7084-0529
Peter Plavchan ⓘ https://orcid.org/0000-0002-8864-1667
Avi Shporer ⓘ https://orcid.org/0000-0002-1836-3120
Hui Zhang ⓘ https://orcid.org/0000-0003-3491-6394
Brendan P. Bowler ⓘ https://orcid.org/0000-0003-2649-2288
Jack Okumura ⓘ https://orcid.org/0000-0002-4876-8540
Markus Rabus ⓘ https://orcid.org/0000-0003-2935-7196
Marshall C. Johnson ⓘ https://orcid.org/0000-0002-5099-8185
Daniel Harbeck ⓘ https://orcid.org/0000-0002-8590-007X
René Tronsgaard ⓘ https://orcid.org/0000-0003-1001-0707
Lars A. Buchhave ⓘ https://orcid.org/0000-0003-1605-5666
Karen A. Collins ⓘ https://orcid.org/0000-0001-6588-9574
Kevin I. Collins ⓘ https://orcid.org/0000-0003-2781-3207
Tianjun Gan ⓘ https://orcid.org/0000-0002-4503-9705
Eric L. N. Jensen ⓘ https://orcid.org/0000-0002-4625-7333
Steve B. Howell ⓘ https://orcid.org/0000-0002-2532-2853
E. Furlan ⓘ https://orcid.org/0000-0001-9800-6248
Crystal L. Gnilka ⓘ https://orcid.org/0000-0002-9903-9911
Kathryn V. Lester ⓘ https://orcid.org/0000-0002-9903-9911
Rachel A. Matson ⓘ https://orcid.org/0000-0001-7233-7508
Nicholas J. Scott ⓘ https://orcid.org/0000-0003-1038-9702
George R. Ricker ⓘ https://orcid.org/0000-0003-2058-6662
Roland Vanderspek ⓘ https://orcid.org/0000-0001-6763-6562
David W. Latham ⓘ https://orcid.org/0000-0001-9911-7388
Joshua N. Winn ⓘ https://orcid.org/0000-0002-4265-047X
Jon M. Jenkins ⓘ https://orcid.org/0000-0002-4715-9460
David R. Rodriguez ⓘ https://orcid.org/0000-0003-1286-5231
Douglas A. Caldwell ⓘ https://orcid.org/0000-0003-1963-9616
Samuel N. Quinn ⓘ https://orcid.org/0000-0002-8964-8377
Zahra Essack ⓘ https://orcid.org/0000-0002-2482-0180
Luke G. Bouma ⓘ https://orcid.org/0000-0002-0514-5538

References

Addison, B., Wright, D. J., Wittenmyer, R. A., et al. 2019, PASP, 131, 115003
Addison, B. C., Wright, D. J., Nicholson, B. A., et al. 2021, MNRAS, 502, 3704

Anglada-Escudé, G., Arriagada, P., Vogt, S. S., et al. 2012, ApJL, 751, L16
Baluev, R. V. 2009, MNRAS, 393, 969
Barnes, S. I., Gibson, S., Nield, K., & Cochrane, D. 2012, Proc. SPIE, 8446, 844688
Blanco-Cuaresma, S. 2019, MNRAS, 486, 2075
Blanco-Cuaresma, S., Soubiran, C., Heiter, U., et al. 2014, A&A, 569, A111
Borucki, W. J., Koch, D., Basri, G., et al. 2010, Sci, 327, 977
Bowler, B. P., Johnson, J. A., Marcy, G. W., et al. 2010, ApJ, 709, 396
Brahm, R., Jordán, A., & Espinoza, N. 2017, PASP, 129, 034002
Brahm, R., Nielsen, L. D., Wittenmyer, R. A., et al. 2020, AJ, 160, 235
Brown, T. M., Baliber, N., Bianco, F. B., et al. 2013, PASP, 125, 1031
Bryant, E. M., Bayliss, D., Nielsen, L. D., et al. 2020, MNRAS, 499, 3139
Buchhave, L. A., Bakos, G. A., Hartman, J. D., et al. 2010, ApJ, 720, 1118
Buchhave, L. A., Bizzarro, M., Latham, D. W., et al. 2014, Natur, 509, 593
Buchhave, L. A., Latham, D. W., Johansen, A., et al. 2012, Natur, 486, 375
Butler, R. P., Marcy, G. W., Fischer, D. A., et al. 1999, ApJ, 526, 916
Ciardi, D. R., Beichman, C. A., Horch, E. P., et al. 2015, ApJ, 805, 16
Clark, J. T., Clerté, M., Hinkel, N. R., et al. 2021, MNRAS, 504, 4968
Cloutier, R., Astudillo-Defru, N., Bonfils, X., et al. 2019, A&A, 629, A111
Cochran, W. D., Hatzes, A. P., Butler, R. P., et al. 1997, ApJ, 483, 457
Collins, K. A., Kielkopf, J. F., Stassun, K. G., & Hessman, F. V. 2017, AJ, 153, 77
Colón, K. D., Kreidberg, L., Welbanks, L., et al. 2020, AJ, 160, 280
Dalba, P. A., Gupta, A. F., Rodriguez, J. E., et al. 2020, AJ, 159, 241
Dawson, R. I., & Johnson, J. A. 2018, ARA&A, 56, 175
Djupvik, A. A., & Andersen, J. 2010, in Highlights of Spanish Astrophysics V, ed. J. M. Diego et al. (Berlin: Springer), 211
Dotter, A. 2016, ApJS, 222, 8
Dotter, A., Chaboyer, B., Jevremović, D., et al. 2008, ApJS, 178, 89
Dreizler, S., Jeffers, S. V., Rodríguez, E., et al. 2020, MNRAS, 493, 536
Foreman-Mackey, D., Hogg, D. W., Lang, D., et al. 2013, PASP, 125, 306
Fortney, J. J., Marley, M. S., & Barnes, J. W. 2007, ApJ, 659, 1661
Gaia Collaboration, Brown, A. G. A., & Vallenari, A. 2018, yCat, 616, A1
Gilbert, J., Bergmann, C., Bloxham, G., et al. 2018, Proc. SPIE, 10702, 107020Y
Goodman, J., & Weare, J. 2010, Comm. App. Math. Comp. Sci., 5, 65
Grunblatt, S. K., Huber, D., Gaidos, E., et al. 2017, AJ, 154, 254
Grunblatt, S. K., Huber, D., Gaidos, E. J., et al. 2016, AJ, 152, 185
Hartman, J. D., Bakos, G. Á., Bhatti, W., et al. 2016, AJ, 152, 182
Hippke, M., David, T. J., Mulders, G. D., et al. 2019, AJ, 158, 143
Hippke, M., & Heller, R. 2019, A&A, 623, A39
Høg, E., Fabricius, C., Makarov, V. V., et al. 2000, A&A, 355, L27
Howell, S. B., Everett, M. E., Sherry, W., et al. 2011, AJ, 142, 19
Huang, C. X., Burt, J., Vanderburg, A., et al. 2018, ApJL, 868, L39
Jenkins, J. M. 2002, ApJ, 575, 493
Jenkins, J. M., Chandrasekaran, H., McCauliff, S. D., et al. 2010, Proc. SPIE, 7740, 77400D
Jenkins, J. M., Twicken, J. D., McCauliff, S., et al. 2016, Proc. SPIE, 9913, 99133E
Jensen, E. 2013, Tapir: A web interface for transit/eclipse observability, Astrophysics Source Code Library, ascl:1306.007
Johnson, J. A., Bowler, B. P., Howard, A. W., et al. 2010, ApJL, 721, L153
Johnson, J. A., Butler, R. P., Marcy, G. W., et al. 2007, ApJ, 670, 833
Jones, M. I., Jenkins, J. S., Brahm, R., et al. 2016, A&A, 590, A38
Jones, M. I., Jenkins, J. S., Rojo, P., et al. 2011, A&A, 536, A71
Jones, M. I., Wittenmyer, R., Aguilera-Gómez, C., et al. 2021, A&A, 646, A131
Jordán, A., Brahm, R., Espinoza, N., et al. 2020, AJ, 159, 145
Kempton, E. M.-R., Bean, J. L., Louie, D. R., et al. 2018, PASP, 130, 114401
Komacek, T. D., Thorngren, D. P., Lopez, E. D., et al. 2020, ApJ, 893, 36
Kotani, T., Tamura, M., Nishikawa, J., et al. 2018, Proc. SPIE, 10702, 1070211
Kreidberg, L. 2015, PASP, 127, 1161
Kunitomo, M., Ikoma, M., Sato, B., et al. 2011, ApJ, 737, 66
Lam, K. W. F., Faedi, F., Brown, D. J. A., et al. 2017, A&A, 599, A3
Lee, E. J., & Chiang, E. 2016, ApJ, 817, 90
Li, J., Tenenbaum, P., Twicken, J. D., et al. 2019, PASP, 131, 024506
Lopez, E. D., & Fortney, J. J. 2016, ApJ, 818, 4
Luque, R., Pallé, E., Kossakowski, D., et al. 2019, A&A, 628, A39

Mahadevan, S., Ramsey, L., Bender, C., et al. 2012, Proc. SPIE, 8446, 84461S
Mamajek, E. E., & Hillenbrand, L. A. 2008, ApJ, 687, 1264
Mayor, M., & Queloz, D. 1995, Natur, 378, 355
McCully, C., Volgenau, N. H., Harbeck, D. R., et al. 2018, Proc. SPIE, 10707, 107070K
Montet, B. T., Morton, T. D., Foreman-Mackey, D., et al. 2015, ApJ, 809, 25
Morris, R. L., Twicken, J. D., Smith, J. C., et al. 2020, Kepler Science Document, KSCI-19081-003
Morton, T. D. 2015, ascl soft, Astrophysics Source Code Library, ascl:1503.010
Nielsen, L. D., Bouchy, F., Turner, O., et al. 2019, A&A, 623, A100
Öberg, K. I., Murray-Clay, R., & Bergin, E. A. 2011, ApJL, 743, L16
Pepe, F., Mayor, M., Queloz, D., et al. 2004, A&A, 423, 385
Pepper, J., Rodriguez, J. E., Collins, K. A., et al. 2017, AJ, 153, 215
Petigura, E. A., Marcy, G. W., Winn, J. N., et al. 2018, AJ, 155, 89
Pollack, J. B., Hubickyj, O., Bodenheimer, P., et al. 1996, Icar, 124, 62
Quinn, S. N., Becker, J. C., Rodriguez, J. E., et al. 2019, AJ, 158, 177
Quirrenbach, A., Amado, P. J., Caballero, J. A., et al. 2014, Proc. SPIE, 9147, 91471F
Reffert, S., Bergmann, C., Quirrenbach, A., et al. 2015, A&A, 574, A116
Ricker, G. R., Winn, J. N., Vanderspek, R., et al. 2015, JATIS, 1, 014003
Rodriguez, J. E., Eastman, J. D., Zhou, G., et al. 2019, AJ, 158, 197
Sato, B., Fischer, D. A., Henry, G. W., et al. 2005, ApJ, 633, 465
Sato, B., Omiya, M., Wittenmyer, R. A., et al. 2013, ApJ, 762, 9
Schlecker, M., Kossakowski, D., Brahm, R., et al. 2020, AJ, 160, 275
Schlegel, D. J., Finkbeiner, D. P., & Davis, M. 1998, ApJ, 500, 525
Sha, L., Huang, C. X., Shporer, A., et al. 2021, AJ, 161, 82
Siverd, R. J., Brown, T. M., Barnes, S., et al. 2018, Proc. SPIE, 10702, 107026C
Skilling, J. 2004, in AIP Conf. Proc. 735, Bayesian Inference and Maximum Entropy Methods in Science and Engineering, ed. R. Fischer, R. Preuss, & U. van Toussaint (New York: AIP Publishing), 395
Smith, J. C., Stumpe, M. C., Van Cleve, J. E., et al. 2012, PASP, 124, 1000
Snellen, I. A. G., Koppenhoefer, J., van der Burg, R. F. J., et al. 2009, A&A, 497, 545
Speagle, J. S. 2020, MNRAS, 493, 3132
Stassun, K. G., Collins, K. A., & Gaudi, B. S. 2017, AJ, 153, 136
Stassun, K. G., Corsaro, E., Pepper, J. A., et al. 2018, AJ, 155, 22
Stassun, K. G., Oelkers, R. J., Paegert, M., et al. 2019, AJ, 158, 138
Stassun, K. G., & Torres, G. 2016, ApJL, 831, L6
Stassun, K. G., & Torres, G. 2018, ApJ, 862, 61
Stumpe, M. C., Smith, J. C., Catanzarite, J. H., et al. 2014, PASP, 126, 100
Stumpe, M. C., Smith, J. C., Van Cleve, J. E., et al. 2012, PASP, 124, 985
Talens, G. J. J., Albrecht, S., Spronck, J. F. P., et al. 2017, A&A, 606, A73
Telting, J., Avila, G., Buchhave, L., et al. 2014, AN, 335, 41
Thorngren, D. P., Fortney, J. J., Lopez, E. D., et al. 2021, ApJL, 909, L16
Torres, G., Andersen, J., & Giménez, A. 2010, A&ARv, 18, 67
Trifonov, T. 2019, ascl soft, Astrophysics Source Code Library, ascl:1906.004
Trifonov, T., Caballero, J. A., Morales, J. C., et al. 2021, Sci, 371, 1038
Trotta, R. 2008, ConPh, 49, 71
Twicken, J. D., Catanzarite, J. H., Clarke, B. D., et al. 2018, PASP, 130, 064502
Twicken, J. D., Clarke, B. D., Bryson, S. T., et al. 2010, Proc. SPIE, 7740, 774023
Van Eylen, V., Albrecht, S., Gandolfi, D., et al. 2016, AJ, 152, 143
Vanderburg, A., Huang, C. X., Rodriguez, J. E., et al. 2019, ApJL, 881, L19
Villaver, E., & Livio, M. 2009, ApJL, 705, L81
Villaver, E., Livio, M., Mustill, A. J., et al. 2014, ApJ, 794, 3
Vogt, S. S., Wittenmyer, R. A., Butler, R. P., et al. 2010, ApJ, 708, 1366
Wang, S., Jones, M., Shporer, A., et al. 2019, AJ, 157, 51
Weiss, L. M., Marcy, G. W., Rowe, J. F., et al. 2013, ApJ, 768, 14
West, R. G., Hellier, C., Almenara, J.-M., et al. 2016, A&A, 585, A126
Wittenmyer, R. A., Butler, R. P., Horner, J., et al. 2020, MNRAS, 491, 5248
Wittenmyer, R. A., Horner, J., Carter, B. D., et al. 2018, arXiv:1806.09282
Wolthoff, V., Reffert, S., Quirrenbach, A., et al. 2021, A&A, submitted
Wright, D. J., Wittenmyer, R. A., Tinney, C. G., et al. 2016, ApJL, 817, L20
Zechmeister, M., & Kürster, M. 2009, A&A, 496, 577
Zhou, G., Huang, C. X., Bakos, G. Á., et al. 2019, AJ, 158, 141